The mechanism of oleic acid deoxygenation to green diesel hydrocarbon using porous aluminosilicate catalysts

Reva Edra Nugraha [a], Hari Purnomo [b], Abdul Aziz [b], Holilah Holilah [c], Hasliza Bahruji [d], Nurul Asikin-Mijan [e], Suprapto Suprapto [b,*], Yun Hin Taufiq-Yap [f,g], Aishah Abdul Jalil [h,i], Hartati Hartati [j], Didik Prasetyoko [b]

[a] Department of Chemical Engineering, Faculty of Engineering, Universitas Pembangunan Nasional "Veteran" Jawa Timur, Surabaya, East Java, 60294, Indonesia
[b] Department of Chemistry, Faculty of Sciences, Institut Teknologi Sepuluh Nopember, Keputih Sukolilo, Surabaya, 60111, Indonesia
[c] Research Center for Biomass and Bioproducts, National Research and Innovation Agency of Indonesia (BRIN), Cibinong, 16911, Indonesia
[d] Centre of Advanced Material and Energy Sciences, Universiti Brunei Darussalam, Jalan Tungku Link, BE 1410, Brunei
[e] Department of Chemical Sciences, Faculty of Science and Technology, Universiti Kebangsaan Malaysia, 43600 UKM Bangi, Selangor, Malaysia
[f] Department of Chemistry, Faculty of Science, Universiti Putra Malaysia, 43400, UPM Serdang, Selangor, Malaysia
[g] Catalysis Science and Technology Research Centre (PutraCat), Faculty of Science, Universiti Putra Malaysia, 43400 UPM Serdang, Selangor, Malaysia
[h] Department of Chemical Engineering, Faculty of Chemical and Energy Engineering, Universiti Teknologi Malaysia, 81310, Skudai, Johor Bahru, Johor, Malaysia
[i] Centre of Hydrogen Energy, Institute of Future Energy, Universiti Teknologi Malaysia, 81310, Skudai, Johor Bahru, Johor, Malaysia
[j] Department of Chemistry, Faculty of Science and Technology, Universitas Airlangga, Surabaya, 60115, Indonesia

ARTICLE INFO

ABSTRACT

The role of mesoporous solid acid aluminosilicate in the oleic acid deoxygenation was elucidated using ZSM-5 and Al-MCM-41 impregnated with Ni. The mesoporous supports were synthesized using a similar initial Si/Al ratio but employing different templates to vary the mesopores. ZSM-5_T produced interparticle mesopores when using TPAOH (tetrapropylammonium hydroxide) as a template. Meanwhile, ZSM-5_S with a well-defined intraparticle mesoporous channel was formed using a silicalite template. Al-MCM-41 synthesized without a template produced one-dimensional highly ordered mesoporous channels. The arrangement of mesoporosity in aluminosilicate determined the mechanistic pathway of oleic acid conversion into hydrocarbon. Oleic acid underwent primary thermal cracking into carboxylic acid before progressing into the subsequent decarbonylation reaction. The diesel hydrocarbon yield was enhanced following the order of Al-MCM-41>ZSM-5_S>ZSM-5_T>blank reaction. Large intraparticle mesoporosity produced long-chain carboxylic acid from catalytic cracking of oleic acid, which was subsequently deoxygenated into long-chain hydrocarbons.

1. Introduction

Renewable biofuel has been extensively investigated as alternative green energy to sustain fossil fuel depletion (Jeon et al., 2019; Wang et al., 2020). The primary component of first-generation biofuel produced from the transesterified biomass is fatty acid methyl esters (FAME) (Ramos et al., 2019; Singh et al., 2020). However, FAME has been reported to have poor thermal and oxidative stability, high viscosity, elevated pour point, elevated cloud point, and decreased heating value (Jeon et al., 2019; Monirul et al., 2015). At high temperatures, the unsaturated bonds in FAME were susceptible to oxidization, causing the oxidative breakdown of biodiesel (Kumar, 2017; Silva et al., 2021). The

oxidation products enhanced the viscosity, consequently shortening biodiesel storage life. Additionally, the high viscosity of biodiesel causes poor atomization and combustion (Unlu et al., 2018). FAME oxidation is detrimental to the engine system as the deposition of carbonaceous coke in the fuel tank can clog the fuel filters and injection systems (Angelovič et al., 2015; Jakeria et al., 2014).

Liquid hydrocarbon from biomass is identified as the second-generation biofuel (Chen et al., 2014; de Barros Dias Moreira et al., 2020; Forghani and Lewis, 2016). Hydrotreatment or deoxygenation reaction produces hydrocarbon by eliminating oxygen in biomass (Janampelli and Darbha, 2021; Shim et al., 2018). Deoxygenation occurs via hydrodeoxygenation, decarboxylation or decarbonylation

processes, producing a different range of hydrocarbon chain lengths (Hermida et al., 2015; Krobkrong et al., 2018). Hydrodeoxygenation uses hydrogen gas at high pressure to reduce oxygenated carbon and unsaturated bonds in biomass, preserving the carbon number (Yoosuk et al., 2019). In decarboxylation (DCO$_2$), the oxygenated carbon fragment was removed as CO$_2$ to produce hydrocarbon with one carbon atom shorter than the fatty acid (Srifa et al., 2014; Yıldız et al., 2020). Deoxygenation can also undergo the decarbonylation (DCO) pathway, in which the oxygen species are removed by releasing carbon monoxide (CO) and water molecules (Janampelli and Darbha, 2021). Since decarboxylation or decarbonylation occurs in the absence of H$_2$ and at atmospheric pressure, the process is advantageous in lowering the operational cost and experimental hazard. DCO$_2$ and DCO also released less water, preventing catalyst deactivation (Krobkrong et al., 2018). Nevertheless, the efficiency of deoxygenation processes is hampered by the competing thermal cracking reaction, producing uncondensed gases and carbonaceous coke.

The catalytic deoxygenation of Ni-based catalysts of oleic acid deoxygenation into hydrocarbon is summarized in Table 1. Three groups of catalysts have been investigated to enhance selectivity towards deoxygenation reaction, i.e., supported sulfide transition metal catalyst, supported noble metal catalyst and supported transition metal catalyst (Chen et al., 2017). Comparison between Os, Ru, Ir, Rh, Ni, Pt, and Pd, a Ni catalyst showed equivalent activity to the noble metal catalysts for the stearic acid deoxygenation reaction (Snåre et al., 2006). Ni provides Lewis acidity to improve liquid hydrocarbon yield while reducing uncondensed gases and carbon char (Nugraha et al., 2021b). The synergy of Ni-Mo sulfide catalyst enhanced oleic acid conversion to C$_{18}$ hydrocarbon while suppressing decarbonylation and decarboxylation pathways (Yoosuk et al., 2019). Compared with Al$_2$O$_3$, the sulfide catalyst has a greater active site density per weight, which increases the catalytic activity for deoxygenation. However, the leaching of sulfur during reactions restricted the reusability and regeneration (Luo et al., 2019). Besides the metal selection, the catalyst support also plays an essential role in the catalytic deoxygenation of fatty acids or triglycerides. The introduction of a hierarchical structure in ZSM-5 enhanced the hydrocarbon yield by up to 65% during the deoxygenation of oleic acid. This increase is attributed to the improved accessibility of acid sites within the hierarchical network (Arumugam et al., 2021). Cu and Ni deposited on H-ZSM-5 have high selectivity towards linoleic acid deoxygenation, suppressing the aromatics formation (Gurdeep Singh et al., 2020). HAlMCM-41 showed superior performance compared to Al-MCM-41 for stearic acid deoxygenation, suggesting that the total acidity of the catalyst is crucial for the reaction (Silva et al., 2018). Ni/Al-MCM-41 demonstrated efficiency in the deoxygenation reaction of fatty acids, achieving the highest percentage of hydrocarbons (78 %) (de Sousa Castro et al., 2020). Using porous solid acid catalysts as Ni support enhanced the diffusion of triglycerides to access Lewis acid

sites, which improved biomass conversion into liquid hydrocarbon (Nugraha et al., 2021a).

This study continues our previous work on mesoporous catalysts for vegetable oil conversion into liquid hydrocarbon via deoxygenation reaction (Nugraha et al., 2021b, 2021a). Several biomasses, such as *Reutelis trisperma* oil and *Jatropha* oil, were converted into liquid hydrocarbon with green diesel compositions (Al Muttaqii et al., 2017; Nugraha et al., 2021a, 2021b; Yulia and Zulys, 2020). The biomasses are susceptible to deoxygenation and thermal cracking reactions, in which a highly ordered mesoporous catalyst enhances the deoxygenation pathway. However, elucidating the reaction mechanism is challenging because C$_{16}$–C$_{18}$ fatty acids in the biomasses produce a wide range of intermediate molecules. Herein, oleic acid was used to probe the mechanism of deoxygenation in solvent-free and H$_2$-free environments while employing Ni/aluminosilicate catalysts with different mesoporous properties. This study aimed to investigate the role of mesoporosity in traversing the molecular pathway of oleic acid deoxygenation and thermal cracking by monitoring the liquid product composition within four hours of the reaction.

2. Experimental

2.1. Materials

Solid acid catalysts were synthesized using kaolin (Al$_4$(Si$_4$O$_{10}$) (OH)$_8$) from Bangka Belitung Island, Indonesia that contained 57 % SiO$_2$ and 22 % Al$_2$O$_3$. TPAOH (40% wt in water), colloidal silica (LUDOX® HS-40, silica in water at 30 %), Ni(NO$_3$)$_2$·6H$_2$O (>98% wt), oleic acid (>99 % purity) and ammonium acetate (CH$_3$COONH$_4$) were purchased from Sigma Aldrich in Germany. NaOH was acquired from Merck in Germany and CTABr (C$_{19}$H$_{42}$BrN, assay 99 %) from Applichem. Silicalite template was synthesized following previously reported procedure (Nugraha et al., 2021a).

2.2. Catalyst synthesis

All solid acid supports were synthesized at Si/Al = 25 ratio with the initial molar composition of 10Na$_2$O:100SiO$_2$: 2Al$_2$O$_3$:1800H$_2$O (Nugraha et al., 2021a). Different types of templates including TPAOH and silicalite, have been employed as structure-directing agents in the synthesis of solid acid supports. These templates are used to modify the aluminosilicate-type structure. The synthesis was also realized with the absence of a template (without a template) in this study. The CTAB is used as a mesopore directing agent for aluminosilicate synthesis. Intraparticle ZSM-5 mesopore was created using silicalite as a template and abbreviated as ZSM-5_S. ZSM-5 with interparticle mesopores was synthesized using TPAOH as a template and labeled as ZSM-5_T. Al-MCM-41 with highly ordered mesopores was obtained without

Table 1
Summary of Ni catalysts activity in oleic acid deoxygenation.

Catalyst	Reaction	Reactor	Reaction condition	Conversion (%)	Hydrocarbon selectivity (%)	Ref.
NiMo/γ-Al$_2$O$_3$	Decarboxylation-decarbonylation (deCOx)	Batch Reactor	T = 300–350 °C, t = 3–9 h	97	57 % (Heptadecane)	(Krobkrong et al., 2018)
Ni/β-Zeolite	Hydrocracking	Micro-scale trickle bed reactor	T = 350–450 °C	71–97	58 (C$_9$–C$_{11}$)	(Forghani and Lewis, 2016)
Ni/ZnO-Al$_2$O$_3$	Hydrodecarbonylation	Batch Reactor (Decalin as solvent)	T = 280 °C, P = 3.5 MPa H$_2$, t = 6 h	100	94.5 (Heptadecane)	(G. Li et al., 2015)
Ni$_2$P/Al-SBA-15	Hydrodeoxygenation (HDO)	Batch Reactor	T = 260–300 °C, t = 6 jam, H$_2$ 50 bar	90	42 (C$_{10}$–C$_{18}$)	(de Oliveira Camargo et al., 2020)
NiO Mesoporous	Hydrodeoxygenation (HDO)	Batch Reactor	T = 300 °C, t = 3 h, H$_2$ 20 bar	100	63 (Heptadecane)	(Smoljan et al., 2020)
Ni-CeZrO$_2$	Deoxygenation	Batch Reactor	T = 300 °C, t = 3 h, P = 1 atm (20 % H$_2$/N$_2$)	98.3	33.9 (C$_9$–C$_{17}$)	(Jeon et al., 2019)
Ni/Al-MCM-41	Decarboxylation-decarbonylation (deCOx)	Semi-batch reactor Solvent-free	P = 350 °C, t = 4 h, N$_2$ (H$_2$-free)	80.29	88.57 (C$_8$–C$_{17}$)	This study

silicalite and TPAOH. The obtained Na-aluminosilicate was converted to the NH_4^+ form by cation exchange with ammonium acetate solution. 1 g Na-aluminosilicate was dispersed in 50 mL ammonium acetate solution (1 M) and vigorously stirred at 80 °C for 3 h. Ni (10% wt) was impregnated to NH_4^+ form of aluminosilicate support via incipient wetness impregnation method using $Ni(NO_3)_2$ solution. The catalyst was dried for 24 h at 120 °C and calcined at 550 °C (heating rate 2°C/min) using N_2 atmosphere for 1 h and continued with air for 6 h. The catalysts were denoted as 10%Ni/ZSM-5_S, 10%Ni/ZSM-5_T and 10% Ni/Al-MCM-41.

2.3. Characterization

The solid acid catalyst was analyzed with low and wide-angle X-ray diffraction. The low X-ray diffraction was used to analyze the ordered arrangement in a mesoporous structure. Meanwhile, wide-angle X-ray diffraction was used to analyze the phase composition in solid acid catalysts. The low-angle X-ray diffraction was measured with Bruker type D2 Phaser diffractometer with KFL Cu 2 K. The X-ray diffraction pattern of each sample were measured with a steps size of 0.020° and scanning with the range of $2\theta = 2$–$10°$ The data were collected with radiation at 10 mA and 30 kV. The wide-angle X-Ray diffraction was measured with Binary XPert from Philips using an MPD Cu K diffractometer which scanned from 5° to 80° The analysis was run at 30 mA, 40 kV with scanned in steps of 0.01670. The functional group was examined using FTIR Shimadzu Instrument Spectrum One 8400S. The Quantachrome Touchwin v1.11 instrument for N_2 Adsorption Desorption was used to determine the surface area and pore volume. Pyridine-FTIR was used to assess the Lewis and Bronsted acidity (Shimadzu Instrument Spectrum One 8400S). The pyridine desorption was conducted at 150 °C for 3 h and analyzed using FTIR at 2000–1400 cm^{-1}. The High Transmission Electron Microscopy (HT-TEM) of the catalysts were recorded using Hitachi HT-7700 TEM operated at 100 kV. Hitachi Scanning Electron Microscope (SEM) Flex SEM 1000 was used to analyze the morphology of aluminosilicates.

2.4. Deoxygenation of Oleic acid

The oleic acid deoxygenation was conducted using a semi-batch reactor under N_2 atmosphere. Oleic acid (10 g) and 3% catalyst were added in a 100 mL three-necked flask equipped with a distillation apparatus and a stirring heating mantle. No solvent is used in the deoxygenation reaction. The mixture was stirred continuously at 350 °C for 4 h. The liquid product was sampled hourly and analyzed using HP 6890 Gas Cromatography-Mass Spectroscopy with HP-5MS Capillary column (30 m x 0.32 mm x 0.25 mm). For the quantitative study, 1-bromohexane was used as an internal standard. The fatty acid (FA) content of the liquid product and RTO were utilized to calculate the degree of deoxygenation (Eq. (1)). To calculate the proportion of liquid yield, Eq. (2) was employed. The selectivity of the hydrocarbon was calculated using Eq.

$$Degree\ of\ deoxygenation = \left[1 - \left(\frac{\%FA\ in\ liquid\ product}{\%FA\ in\ reactant}\right)\right] \times 100\%$$

$$(1)$$

$$Liquid\ yield = \left(\frac{weight\ of\ liquid\ product}{weight\ of\ reactant}\right) \times 100\%$$

$$(2)$$

$$Selectivity = \frac{(peak\ area\ of\ desired\ hydrocarbon)}{(peak\ area\ of\ total\ hydrocarbon)} \times 100\%$$

$$(3)$$

2.5. Coke analysis

TGA analysis of carbonaceous coke on the spent catalyst was determined using Linseis STA PT-1000. The analysis was conducted in air at

50–600 °C with a heating rate of 10 °C/min. Low-angle XRD analysis was also conducted to determine the deposition of carbonaceous coke on mesopores using D2 Phaser type, Bruker XRD with KFL Cu 2 K in the range $2\theta = 1.5$–$10°$ at 10 mA and 30 kV radiation.

3. Results and discussion

3.1. Catalyst characterization

3.1.1. XRD analysis

The XRD of 10%Ni/ZSM-5_S and 10%Ni/ZSM-5_T showed highly intense XRD peaks at $2\theta = 7.8, 8.7, 23, 23.8$ and 24° assigned to the MFI framework of ZSM-5 according to JCPDS database No. 44–0003 (Fig. 1) (Feng et al., 2019). However, 10%Ni/Al-MCM-41 shows a broad peak between 15°–30°, indicating the formation of amorphous aluminosilicate (Nugraha et al., 2021b; Tran et al., 2016). NiO was identified based on the peaks at $2\theta = 37.11°$ (111), 43.07° (200) and 62.52° (220) (JCPDS 01-075-0197) (Baharudin et al., 2020, 2019). No other peaks were detected in XRD analysis, indicating the synthesis successfully transformed kaolin to a relatively pure phase Al-MCM-41 or ZSM-5. The low angle XRD in Fig. 1b exhibits an intense peak at $2\theta = 2.2°$ corresponding to the (100) diffraction plane and a weak diffraction peak at 4.43° assigned to (200) diffraction plane. The peaks confirmed the development of highly ordered hexagonal mesostructure of Al-MCM-41 (Li et al., 2013; Silva et al., 2018). Concurrently, the absence of diffraction peaks at $2\theta = 2$–$5°$ for ZSM-5 catalysts indicates the absence of ordered hexagonal pore structures.

3.1.2. Pyridine-FTIR analysis

The surface acidity of the catalyst was assessed by FTIR analysis with pyridine as a probe molecule (Fig. 2). The catalysts were saturated with pyridine at ambient temperature, and the desorption of physisorbed pyridine was conducted at 150 °C (Riyanto et al., 2021). The Brønsted acid sites can be identified from the adsorption peak at 1540 cm^{-1}. Meanwhile, the characteristic absorption band of the Lewis acid appeared at 1450 cm^{-1} (Li et al., 2016). All the catalysts demonstrated a higher density of Lewis acid than Brønsted acid. 10 % Ni/Al-MCM-41 has 0.499 mmol/g Lewis acid sites, followed by 10 % Ni/ZSM-5_T at 0.377 mmol/g and 10 % Ni/ZSM-5_S at 0.320 mmol/g (Table 2). NiO increased the acidity of aluminosilicate support by providing the additional Ni^{2+} Lewis acidity (Baharudin et al., 2019). The Lewis acidity was also increased by the proton exchange of the Si-O-Al framework with the Ni^{2+} ion (Moussa et al., 2020). The 10 %Ni/Al-MCM-41 catalyst also showed a higher concentration of Brønsted acidity at 0.167 mmol/g compared to 10 %Ni/ZSM-5_T and 10 %Ni/ZSM-5_S. Lewis and Brønsted acids are essential to catalyze deoxygenation reactions (Baharudin et al., 2020).

3.1.3. N_2 adsorption-desorption analysis

Fig. 3a shows the type IV isotherm with a hysteresis loop, a typical isotherm for mesoporous materials. However, rapid N_2 adsorption at low P/P_0 indicates the Langmuir nitrogen adsorption in the micropores. MCM-41 exhibited micropore and mesopore properties, with the 10 % Ni/Al-MCM-41 having micropore surface area of 168.76 m^2/g and micropore pore volume of 0.11 cc/g. These results were in accordance with previous study which showing the micropore and mesopore characteristic in MCM-41 (Oliveira et al., 2023; Pham et al., 2020; Solmaz et al., 2011). The large mesopores are connected to the external surface through narrow, bottleneck-shaped channels in micro-mesoporous materials. Therefore, the mesopores were continuously filled during the N_2 adsorption and desorption process until the N_2 in the narrow channels was completely desorbed at lower vapor pressures (Oliveira et al., 2023; Thommes et al., 2015). A rapid N_2 uptake at higher P/P_0 resulted from the capillary condensation and N_2 multilayer adsorption. These findings validated the hierarchical micropore and mesopore structures in all the catalysts, as summarized in Table 2. Al-MCM-41 catalyst demonstrated a
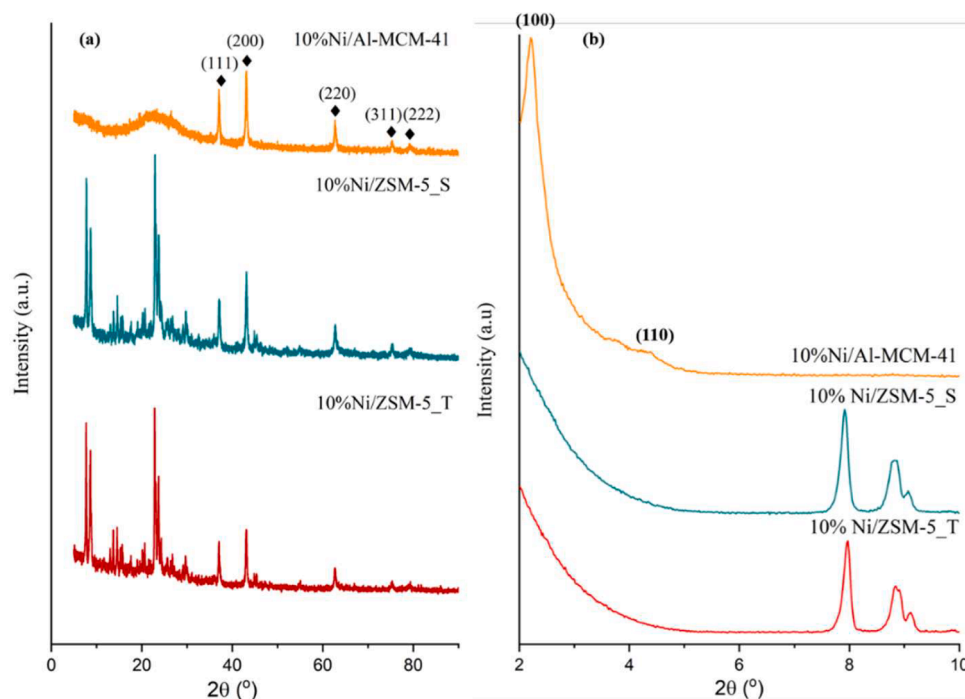
Fig. 1. The diffractogram of (a) wide and (b) low angle of aluminosilicate catalysts.
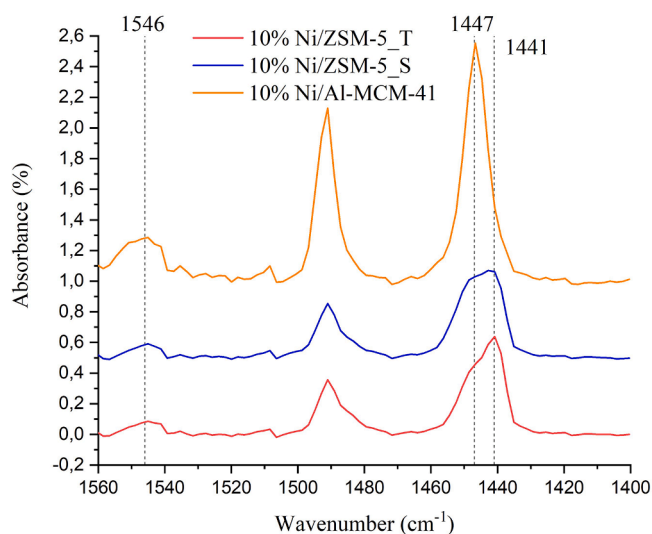

Fig. 2. FTIR pyridine spectra of all catalysts.

substantial increment in nitrogen uptake at relative pressure between 0.3 to 0.4 as a result of the capillary condensation of N_2 in the hexagonal mesopores (Cakiryilmaz et al., 2019; Du and Yang, 2012; Jafarzadeh et al., 2016). The 10 % Ni/Al-MCM-41 presents a large surface area

(398.326 m^2/g) and pore volume (0.448 cc/g). Meanwhile, the porosity in 10 %Ni/ZSM-5_T and 10%Ni/ZSM-5_S predominantly existed in the mesopore region with a low micropore surface area (<40 m^2/g). The differences in textural properties are associated with the effect of organic templates that lead to various mesopore structures. The template enhanced the crystallinity of aluminosilicate to form a ZSM-5 framework, consequently reducing the mesoporosity. Mesoporosity increased from 10%Ni/ZSM-5_T < 10%Ni/ZSM-5_S < 10 % Ni/Al-MCM-41. The mesopore is still visible despite impregnation with 10 % NiO with bimodal pore widths between 2.5 and 6.0 nm (Fig. 3b).

3.1.4. SEM analysis

Fig. 4 shows the SEM analysis and Ni elemental mapping of the catalysts. The 10%Ni/ZSM-5_S formed rod-like crystallite with particle diameters of 0.91 to 1.22 μm. However, the 10%Ni/ZSM-5_T demonstrated the cubic-shaped structures with particle diameters between 1.01 and 1.28 μm. The amorphous 10%Ni/Al-MCM-41 displayed non-uniform crystallites. The elemental composition from EDX analysis shows the Ni composition ranges from 7.25 to 10.57 %, which is in agreement with the experimental value(Table 3 and **Fig. S1**). The EDX elemental mapping of NiO showed heterogeneous dispersion of NiO on the support, leading to poor distribution of NiO particles.

3.1.5. TEM analysis

TEM analysis identified the ordered parallel mesopore channels of solid acid support and the distribution of NiO nanoparticles. NiO

Table 2
Physicochemical properties of Ni/aluminosilicate.

Samples	Surface area (m^2/g)			Pore volume (cc/g)			V_{meso}/V_{micro}	D_{micro}	D_{meso}	Number of acid sites (mmol/g)		Lewis density (μmol/m^2)
	S_{BET}[a]	S_{meso}	S_{micro}[b]	V_{total}	V_{meso}	V_{micro}[b]				Lewis	Brønsted	
10%Ni/ZSM-5_T	196.80	159.83	36.97	0.28	0.24	0.04	6	1.36	2.97, 5.06	0.377	0.042	1.91
10%Ni/ ZSM-5_S	226.88	187.35	39.53	0.29	0.25	0.04	6.25	1.45	2.88, 5.09	0.320	0.043	1.41
10%Ni/Al-MCM-41	398.33	229.57	168.76	0.47	0.36	0.11	3.27	–	3.57	0.499	0.167	1.25

[a] S_{BET} was calculated with BET method.

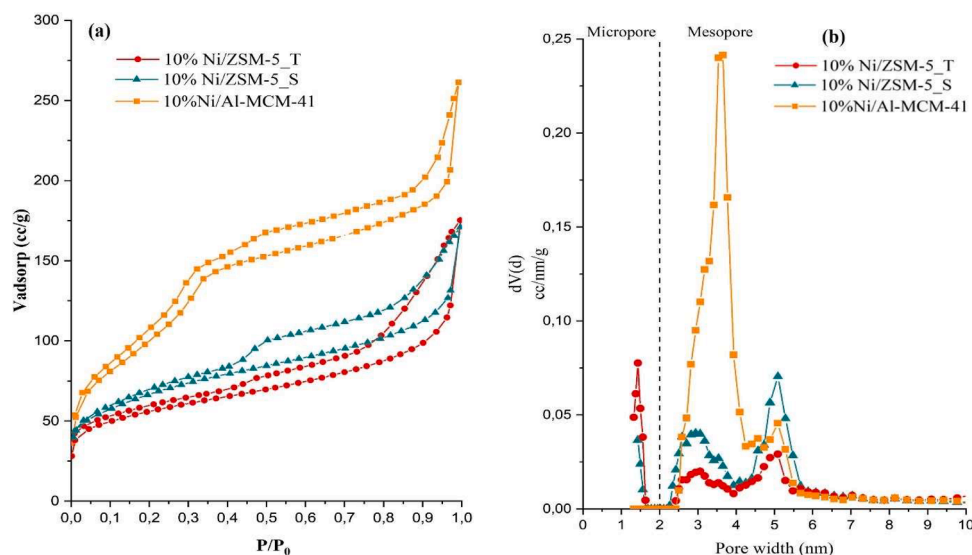[b] S_{micro} and V_{micro} measured with t-plot method.

Fig. 3. N₂ isotherm (a) and NLDFT pore size distribution (b) of 10 %Ni/aluminosilicate.

nanoparticles at ∼ 30 nm diameter were deposited on the external surface of ZSM-5_S (Fig. 5**a**). ZSM-5_S indicated the emergence of rod-like structures with 850 nm-sized particle sizes, as previously observed in SEM analysis (Fig. 5**b**). 10%Ni/ZSM-5_T showed NiO nanoparticles distribution on the surface with 35–40 nm diameter (Fig. 5**c**). The 10% Ni/ZSM-5_T formed cubic-like structures with particle sizes of ~800 nm (Fig. 5**d**). The ordered mesoporous structure was negligible in ZSM-5_T, and therefore the mesoporosity appeared in the N₂ adsorption-desorption analysis was mainly originated from the interparticle interaction between zeolite crystallites. The TEM analysis of 10%Ni/Al-MCM-41 displayed the construction of one-dimensional mesopore channels. NiO nanoparticles were deposited on the surface at ~16–30 nm diameter (Fig 5**e,f**). As confirmed by low angle XRD analysis, the ordered mesoporous channel of Al-MCM-41 demonstrated the remarkable regularity of mesopores.

3.2. Catalytic activity

The final products collected from the oleic acid catalytic deoxygenation at 350 °C for 4 h were divided into uncondensed gases, liquid yield and carbon char. Blank reaction without a catalyst showed 48.8 % conversion of oleic acid. However, only 17.5 % of the converted oleic acid was liquid, 28.3 % was uncondensed gases and 3 % was carbon char (Table 4). Ni/Al-MCM-41 catalyst enhanced oleic acid conversion to 80.3 %, producing 37.7 % liquid product. Ni/ZSM-5_S also improved oleic acid conversion to 60 %, with 25.5 % liquid yield. However, Ni/ZSM-5_T showed approximately similar activity with the blank reaction, at 52.2 % conversion to give 19.2 % liquid yield. Despite all the catalysts having acidity for the deoxygenation reaction (Abdulkareem-Alsultan et al., 2020; Abidin et al., 2019), the differences in product selectivity implied the mesopores effect in converting oleic acid to liquid products.

GCMS analysis of the liquid yield revealed that hydrocarbon is the main product of the deoxygenation reaction at 350 °C after 4 h of reaction (Fig. 6). Hydrocarbon yield is enhanced when using Ni/Al-MCM-41, followed by Ni/ZSM-5_S, and Ni/ZSM-5_T. The cycloalkane, aromatic, ketone, and alcohol were also analyzed as side products. The cycloalkane, ranging from cyclopentane (C_5H_{10}) to undecyl cyclohexane ($C_{17}H_{34}$), was produced below 10 % yield, resulting from the cyclization of hydrocarbon. The aromatic compound was also produced as a side product with less than 5 % composition. Blank reaction and Ni/ZSM-5_T produced short-chain carboxylic acid, indicating inefficient deoxygenation of oleic acid. Lewis acid catalyzes the deoxygenation of oleic acid,

but it also catalyzes thermal cracking to produce short-chain hydrocarbon and uncondensed gas, reducing liquid yield production. Mesoporous catalysts reduced the diffusion path for the oleic acid to access acid sites, consequently increasing the diffusivity of reactants and the resulting products (Alaba et al., 2016). The large intraparticle mesopores provide facile transportation of product and reactant for efficient mass transfer during deoxygenation, improving the catalyst stability and reducing coke formation (Alaba et al., 2016; Palizdar and Sadrameli, 2020). Although Ni/ZSM-5_T displayed mesoporosity from interparticle interactions, there is a possibility that such interactions are destroyed upon the dispersion of catalysts in oil, thus lowering the catalytic activity.

Green diesel consists of hydrocarbons such as aliphatic hydrocarbon (alkane and alkene) as a main component, with a mixture of cyclic and aromatic compounds (Chen et al., 2017). Although cyclic and aromatic compounds were classified as hydrocarbons, the composition in green diesel should minimize since the difficulty of a complete combustion compared to aliphatic hydrocarbons. This incomplete combustion leads to higher emissions of particulate matter (PM), carbon monoxide (CO), and other harmful pollutants, contributing to air pollution and smog formation (Hakkarainen et al., 2023; Neill et al., 2000). Cyclic hydrocarbons have higher boiling points and lower cetane numbers than straight-chain alkanes (Abozenadah et al., 2017; Huo et al., 2019). Higher boiling points can lead to poor cold flow properties, while lower cetane numbers can result in poorer ignition quality.

3.2.1. Effect of reaction time

The mechanistic pathway of oleic acid deoxygenation is shown by analyzing the composition of liquid products at various reaction durations. Continuous hydrocarbon production up to 4 h was accompanied by the reduction of carboxylic acids (Fig. 7). Fig. 8 present the hydrocarbon and carboxylic composition after oleic acid deoxygenation for 1–4 h. The hydrocarbon composition was divide in to gasoline (C7-C10) and diesel (C11–18) range. The longer reaction times result in higher quantities of diesel being produced. Interestingly, short-chain carboxylic acids (C4-C10) were the main product of blank reaction indicating the thermal cracking of oleic acid proceeded before deoxygenation. Ni/ZSM-5_T also contained a high composition of short-chain carboxylic acids at 1 h, suggesting that thermal cracking of oleic acid also occurs on Ni/ZSM-5_T. Carboxylic acids were also observed on ZSM-5_S and Al-MCM-41. However, the acids contained C_{14}–C_{16} carbon number. The detais composition of carboxylic acid was provided in **Table S1-S4**. Although thermal cracking of oleic acid cannot be entirely suppressed,
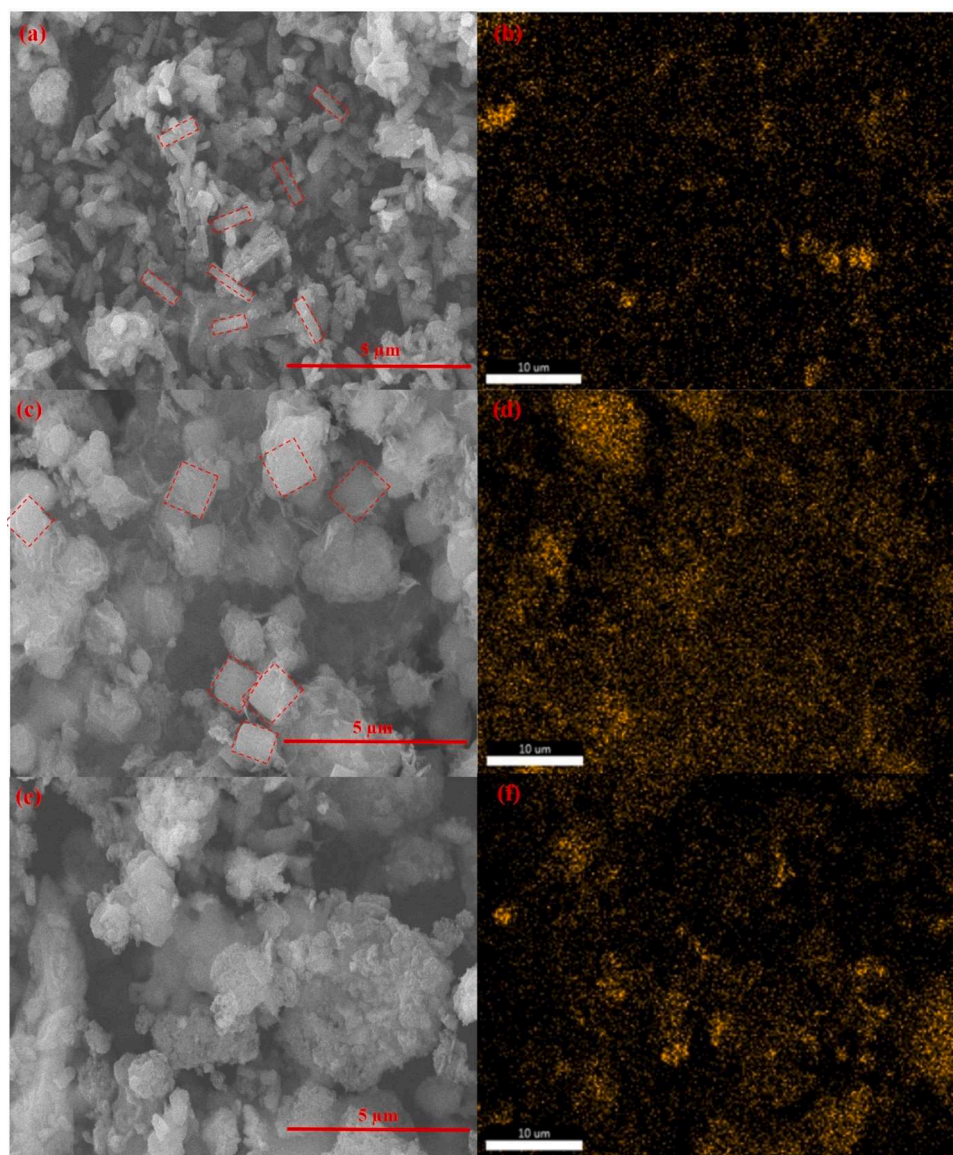
Fig. 4. SEM images and Ni distribution of the 10%Ni/ZSM-5_S (a,b), 10%Ni/ZSM-5_T (c,d) and 10%Ni/MCM-41 (e,f).

Table 3
The EDX analysis of 10%Ni/Aluminosilicate catalysts.

Element	10%Ni/ZSM-5_S	10%Ni/ZSM-5_T	10%Ni/Al-MCM-41
O	56.41	48.25	51.80
Si	3.36	3.89	5.35
Al	32.98	37.29	33.00
Ni	7.25	10.57	9.85

intraparticle mesopores preserved the carbon chain length, which is crucial for forming green diesel hydrocarbon. The dissociated carboxylic acid was eventually converted into hydrocarbon via deoxygenation after 4 h.

The impact of reaction time on hydrocarbon distribution showed that increasing the reaction time enhanced the production of long-chain C_{11}–C_{18} hydrocarbons. The composition of diesel-range hydrocarbon ($C_{11–18}$) were increased from Blank < 10%Ni/ZSM-5_T < 10%Ni/ ZSM-5_S < 10%Ni/Al-MCM-41. Thermal cracking of oleic acid in a blank reaction produced a mixture of short and long-chain hydrocarbons. On the other hand, mesoporous acid catalyst favored the decarboxylation/ decarbonylation pathway to form long-chain hydrocarbon. The alkane/

alkene ratios in Table 4 and **Fig. S2** showed that the amount of alkane produced relative to alkene hydrocarbon was increased with enhanced mesoporosity. A higher amount of alkane/alkene ratio implied the hydrogenation of the unsaturated bond using *in-situ* generated H_2 gas, presumably from the water gas shift reaction (WGSR) between CO and H_2O (Asomaning et al., 2014; Xing et al., 2018). Despite having similar NiO loading, catalysts with interparticle mesoporosity ZSM-5_T showed no significant improvement in converting oleic acid into longer chain molecules.

FTIR analysis was used to describe the liquid product from the 10% Ni/Al-MCM-41 catalyst and the oleic acid (Fig. 9). The stretching vibration of =CH alkenyl was present in the FTIR spectra of oleic acid at 3009 cm^{-1}, as well as the bending vibrations of the = CH alkene at 1454 cm^{-1} and the -CH alkane at 718 cm^{-1} (Niu et al., 2017; Nugraha et al., 2021a; Premaratne et al., 2014). Alkenyl absorbance band reduction in the deoxygenated liquid shows that the unsaturated C=C bond in oleic acid was hydrogenated to produce an aliphatic hydrocarbon (Hossain et al., 2018). The band at 2800–3000 cm^{-1} region primarily indicates the aliphatic functional group. The asymmetric stretching of C—H in the CH_2 hydrocarbon chain was observed at 2932 cm^{-1}. Meanwhile, the band at 2856 cm^{-1} was correlated to the symmetric stretching of -CH_2
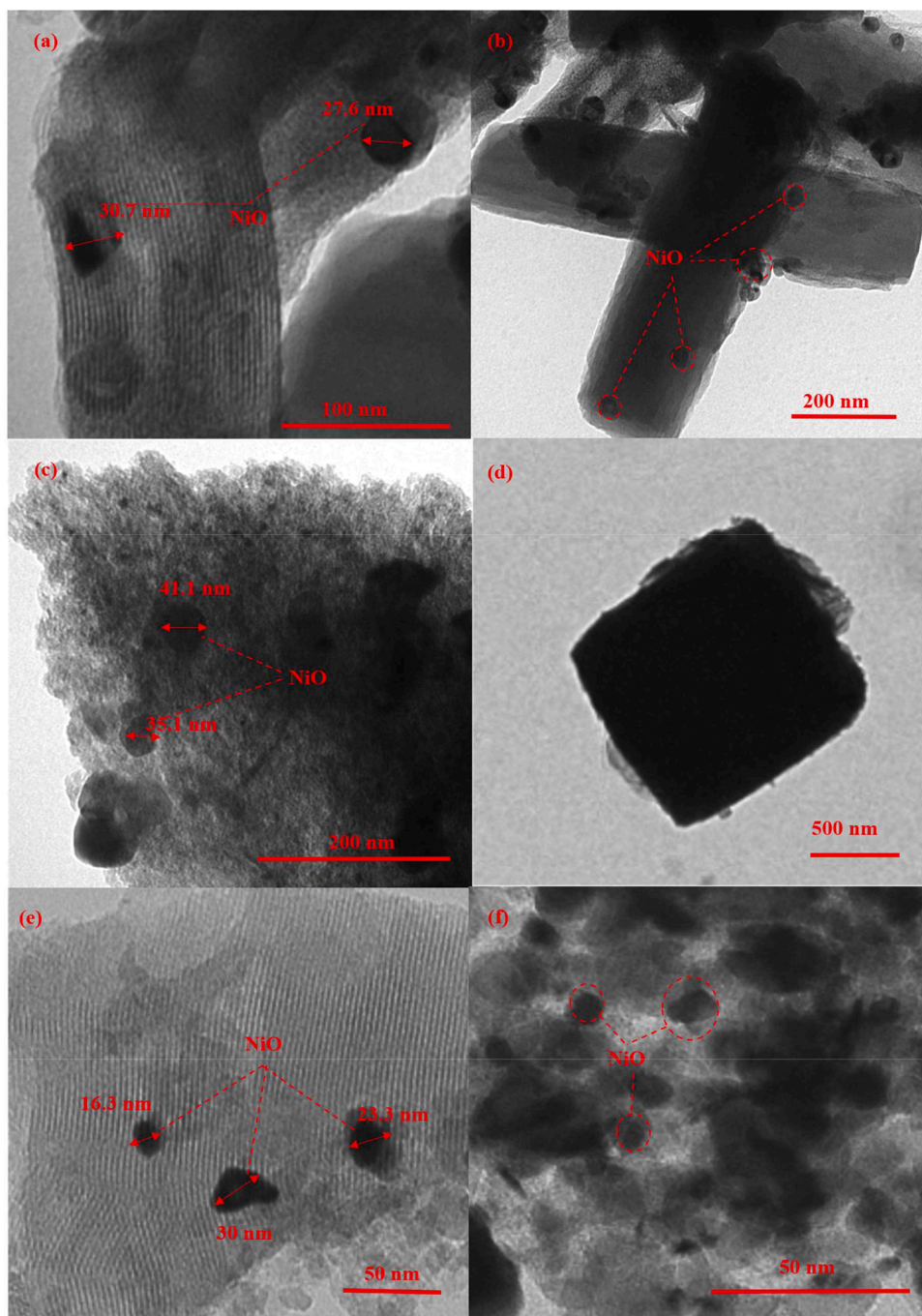
Fig. 5. TEM images of the 10%Ni/ZSM-5_S (a,b), 10%Ni/ZSM-5_T (c,d) and 10%Ni/Al-MCM-41 (e,f).

Table 4
The oleic acid deoxygenation using different mesoporosity catalysts.

Catalysts	$X_{oleic\ acid}$%	Liquid yield,%	$S_{Hydrocarbon}$,%	$S_{Carboxylic\ acid}$,%	C_8–C_{10} yield,%	C_{11}–C_{18} yield,%	Alkane/Alkene ratio
Blank	48.8	17.5	70.37	12.30	3.1	9.3	1.8
Ni/ZSM-5_T	52.2	19.2	81.80	0.43	1.8	13.8	2.0
Ni/ZSM-5_S	60.0	25.5	84.87	0	3.8	17.2	2.2
Ni/Al-MCM-41	80.3	37.7	88.57	0	7.6	25.8	2.5

methylene chain hydrocarbon (Corsetti et al., 2017; Guanhua et al., 2019). The liquid product obtained after the deoxygenation reaction displayed the shift of 2898 m^{-1} and 2822 cm^{-1} bands to lower wavenumber, suggesting the changes in C—H bond length from the different electronegativity of the neighboring atoms (Rodrigues and Shende, 2020). The decreasing of C=O band intensity at 1710 cm^{-1}, stretching vibration of C—O bands at 1292 cm^{-1}, O—H stretching out of plane at 932 cm^{-1} further evidenced the decarboxylation and decarbonylation of the oxygenated carbon in oleic acid.
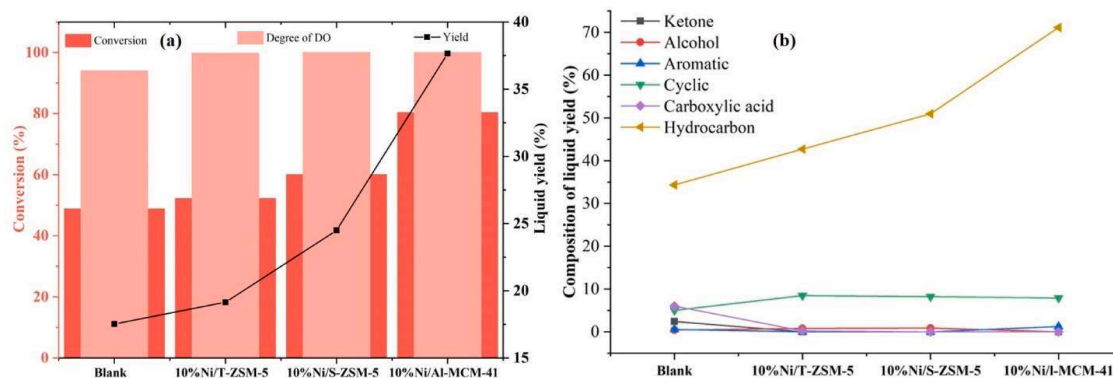
Fig 6. Conversion, yield of oleic acid catalytic deoxygenation (a) and product distribution of deoxygenated liquid product (b).
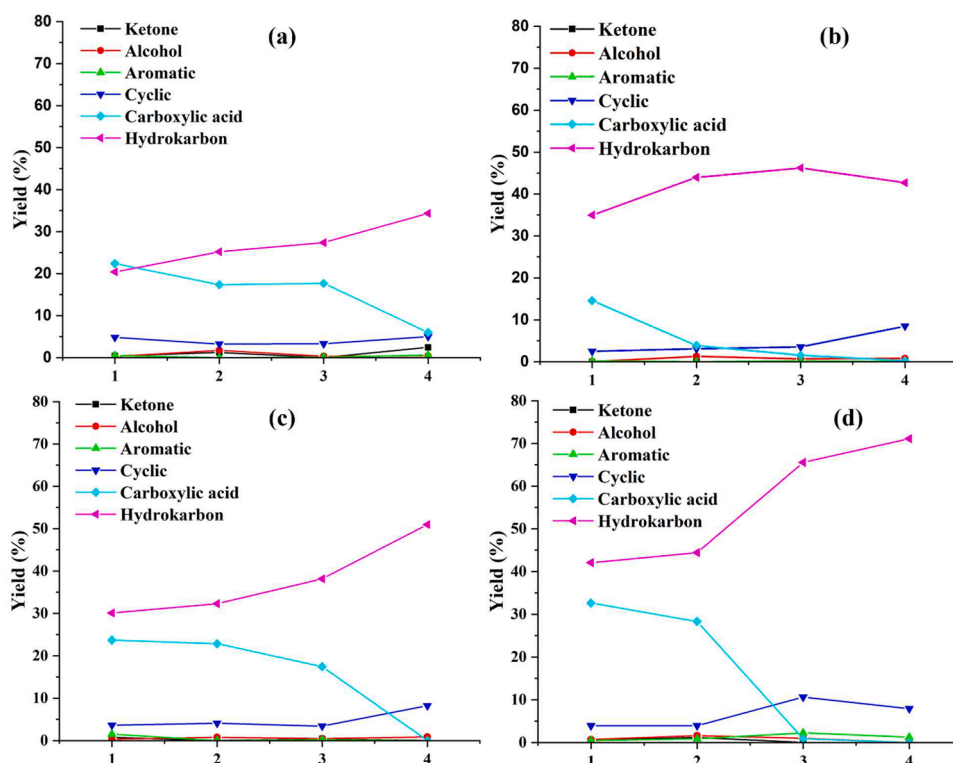

Fig. 7. The composition liquid yield from oleic acid deoxygenation from Blank reaction (a), catalyst 10%Ni/ZSM-5_T (b), 10%Ni/ZSM-5_S (c) and 10%Ni/Al-MCM-41 (d) at 350 °C.

### 3.3. Proposed reaction mechanism

A high density of mesopores increased the yield of diesel-like hydrocarbon by providing an efficient diffusion pathway and acidity for the deoxygenation of fatty acid (Li et al., 2015; Roh et al., 2011). Fig. 10 illustrates the proposed mechanism of oleic acid deoxygenation using Ni/aluminosilicate catalyst. Oleic acid underwent several reaction pathways, i.e., decarboxylation-/decarbonylation (deCOx), hydrogenation and/or thermal cracking depending on the porosity of the catalysts (Krobkrong et al., 2018; Xing et al., 2018). Lewis acid promotes thermal cracking following the carbonium/carbenium ion mechanism. The Lewis acid sites on the catalyst interacted with the double bond of oleic acid to create the carbenium ion (Corma and Orchille, 2000). The carbenium ion is rearranged through a 1,2-hydrogen shift to dissociate the C=C bond and desorbed as short-chain hydrocarbon and carboxylic acid. However, there is potential for the carbenium ion to dissociate, forming smaller molecules, as observed on the blank reaction and the

interparticle mesopore ZSM-5_T. Thermal cracking dissociates the carbon chain favorably through β-scission near the C=C bond, generating shorter carboxylic acid (Maher and Bressler, 2007). When the reaction was carried out using Ni/ZSM-5_T, which has interparticle mesopores, oleic acid diffused slower, thus promoting thermal cracking into short-chain oleic acid.

The high composition of short-chain oleic acid within the first 3 h of the reaction compared to hydrocarbon suggests the thermal cracking reaction occurs faster than the deoxygenation reaction. Although Ni/ZSM-5_T favors thermal cracking reaction, the disappearance of carboxylic acid at four hours of reaction provides evidence of the ability of Lewis acidity to catalyze deoxygenation to form hydrocarbon. The carboxylic acid is diffused into the micropores for deoxygenation reaction, resulting in shorter chain hydrocarbon molecules.

Well-defined mesopores enhanced oleic acid diffusion to deoxygenate -COOH fragments via the deCOx pathway (Hermida et al., 2015; Hongloi et al., 2021). In the deoxygenation reaction, Lewis acid
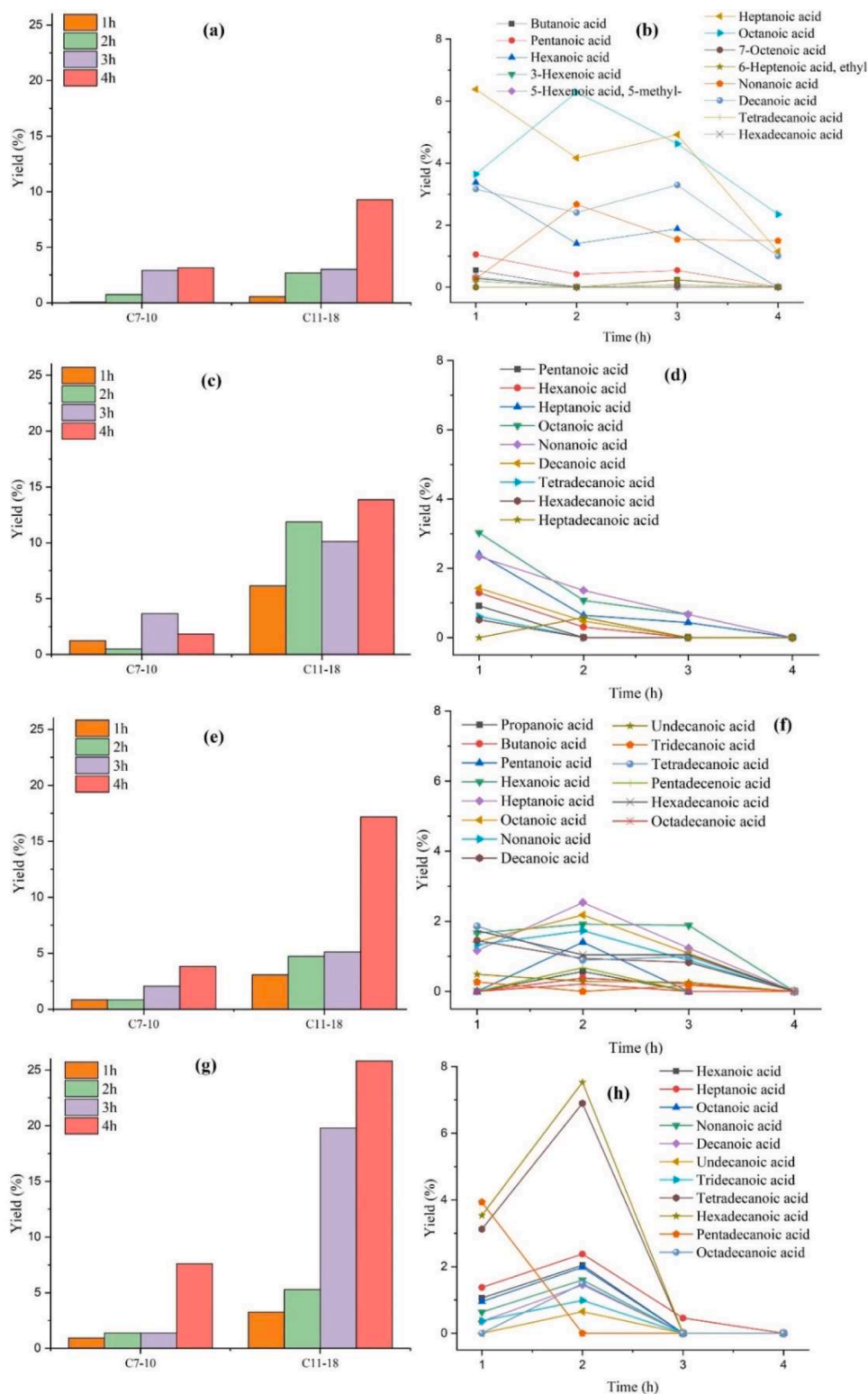
Fig. 8. The hydrocarbon (left) and carboxylic acid (right) composition for blank reaction (a,b), catalyst 10%Ni/ZSM-5_T (c,d), 10%Ni/ZSM-5_S (e,f) and 10%Ni/Al-MCM-41 (g,h) at 350 °C.

interacted with the electron pair of the oxygenated carbon, consequently weakening the C—COOH bond. Catalysts containing a high density of Brønsted acid sites formed strong interactions with olefins, prolonging the lifetime of the carbenium ion. This interaction leads to the formation of cracking products (Wang et al., 2015). As shown in Tables 2 and 4, 10%Ni/Al-MCM-41 with higher Brønsted acid sites would produce two

times higher cracking product of C_8–C_{10} compared to blank reaction and Ni/ZSM-5-based catalyst. A large mesopore channel enhanced the diffusion of $deCO_x$ products from the catalyst surface, thus inhibiting thermal cracking into shorter hydrocarbon. Ni/Al-MCM-41 also formed a higher ratio of alkane/alkene (Table 4), suggesting hydrogenation of the resulting alkene products. Eliminating -COOH functional group via
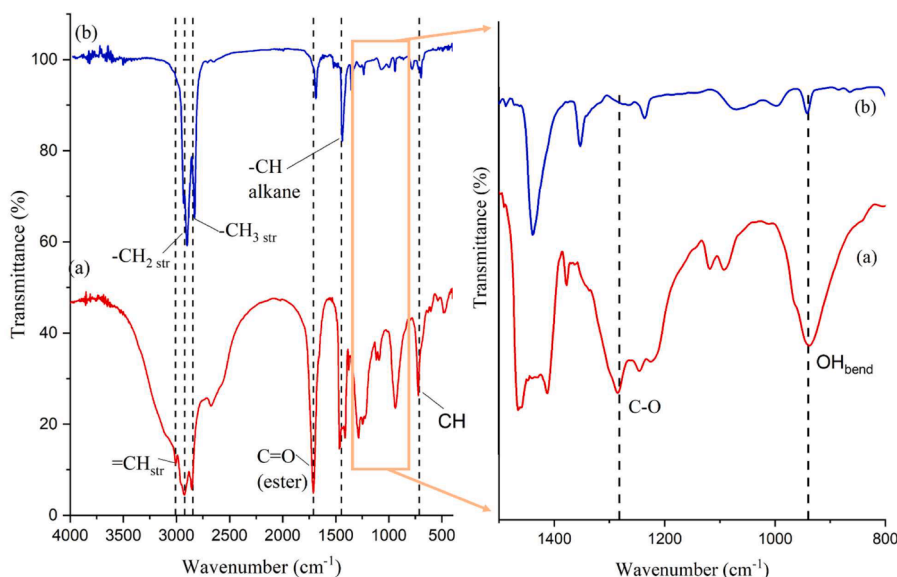
Fig. 9. Oleic acid (a) and deoxygenated liquid product (b) FTIR spectra over a 4 h reaction employing 10% Ni/Al-MCM-41.
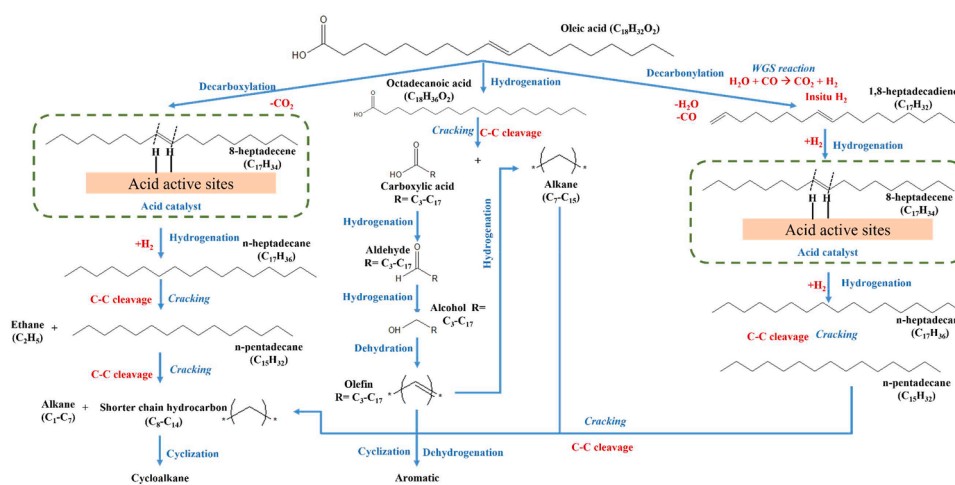

Fig. 10. Proposed reaction mechanism for oleic acid deoxygenation using mesoporous acid catalyst 10%Ni/aluminosilicate.

the decarboxylation route released CO_2 gases and produced alkane (Hermida et al., 2015; Janampelli and Darbha, 2021; Santos et al., 2020). Meanwhile, alkene or olefin was produced via decarbonylation of fatty acid by releasing CO and H_2O side products or by dehydration of alcohol (Ainembabazi et al., 2020; Ali and Zhao, 2020; John et al., 2016). It is hypothesized that the water gas shift interaction (WGSR) between CO and H_2O causes in-situ H_2 production (Asomaning et al., 2014; Xing et al., 2018). The C═C bond hydrogenation using in-situ H_2 that is produced from WGSR may happen since the deoxygenation reaction was performed without the presence of H_2 gas. Notably, octadecanoic acid ($C_{18:0}$) or stearic acid was analyzed on Ni/Al-MCM-41 and Ni/ZSM-5_S during the first three hours of the reaction, which suggested direct hydrogenation of oleic acid occurred prior to deoxygenation. During the cracking reaction, the isomerization and hydride transfer further transformed the shorter-chain hydrocarbon into cycloalkane compounds (Kochaputi et al., 2019; Li et al., 2019).

3.4. Analysis of coke deposit

3.4.1. FTIR and low-angle XRD analysis

Analysis of catalysts recovered from deoxygenation reaction

provides information on the coke deposition. The reduced intensity of the (100) peak seen in the small angle diffractogram pattern of 10% Ni/Al-MCM-41 spent catalyst suggested that carbonaceous coke deposition was occurring in the uniformly hexagonal pore of Al-MCM-41. The (100) peak, however, is still discernible, demonstrating the durability of mesopores throughout the reaction. The reduced peak intensity of the spent catalyst at $2\theta = 7.8$ and $8.7°$ indicates the coke production during the reaction, which covered the surface and micro-mesopores of the ZSM-5 catalyst after the reaction (He et al., 2021). Coke deposition within the pore reduced reactant diffusion and blocked access to active sites (Ooi et al., 2019). FTIR analysis further characterized the coke formation and identified the type of carbonaceous coke (Fig. 11). The specific region of coke characterization is in the range of 1300–1700 cm^{-1} and 2800–3100 cm^{-1} (Aghamohammadi et al., 2019; Li et al., 2015; Zhang et al., 2014). The stretching vibration of C═C in poly-condensed aromatic rings is reflected in the vibration bands at 1467 and 1695 cm^{-1}. The bands at 2867 and 2953 cm^{-1} correspond to the stretching vibration of C─H in aliphatic coke. The results showed that aromatic and aliphatic carbon coke were generated during deoxygenation (Deng et al., 2022).
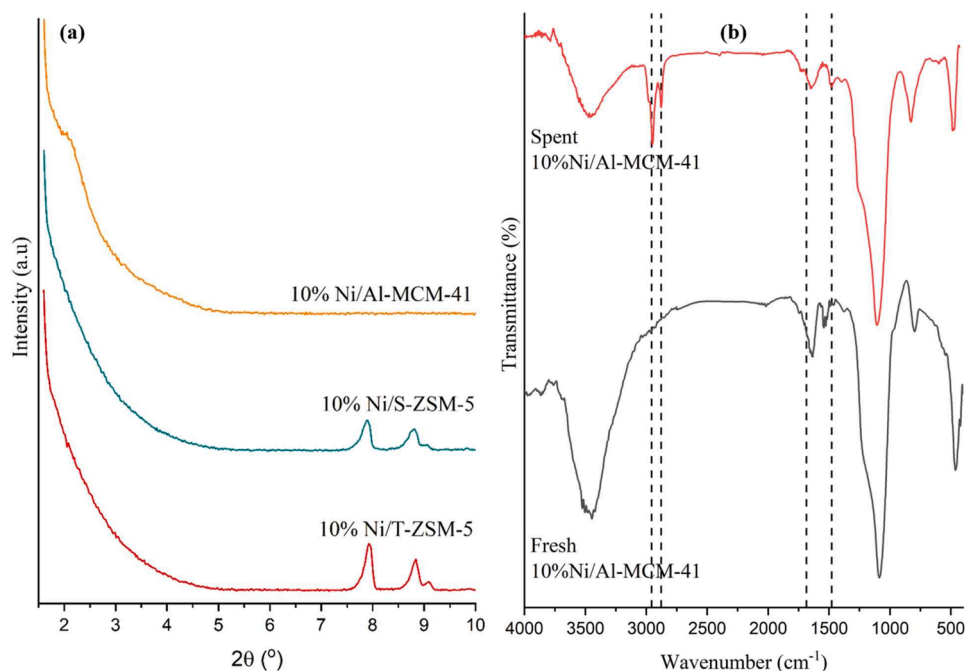
Fig. 11. Low angle X-ray diffraction pattern of spent catalyst (a) and FTIR spectrum of 10%Ni/Al-MCM-41 (b).

3.4.2. TGA-DTG-DTA analysis

The quantity of carbonaceous coke was determined using a thermogravimetric analysis of spent 10%Ni/Al-MCM-41 catalyst in an air atmosphere (Fig. 12). At temperature below 250 °C, 3.62 % of total weight loss was observed, which matched the elimination of physisorbed water on the catalyst. The two exothermic DTA peaks at 300–600 °C indicated the presence of soft/thermal and hard/catalytic carbonaceous coke mixture (Nugraha et al., 2021a). The spent catalyst exhibited 7.94% total weight loss from aliphatic hydrocarbon (soft-/thermal coke) oxidation to CO_2 gas (Crawford et al., 2019). At high temperatures (400–600 °C), 35.5% of total weight loss was measured from the oxidation of polyaromatic carbon (hard/catalytic coke) (Asikin-Mijan et al., 2020; Ma et al., 2016; Techopittayakul et al., 2019). Despite the fact that Lewis acidity boosts the dissociation of C—C bonds

in the thermal cracking and deoxygenation process, it can also stimulate the creation of carbon coke on the catalyst (Tan et al., 2019).

4. Conclusion

The role of mesoporosity of aluminosilicate catalysts was elucidated in oleic acid conversion to green diesel hydrocarbon. Nickel enhances the acidity of aluminosilicates, which promotes oxygen adsorption in the carboxylic group during the deoxygenation reaction. Thermal cracking of oleic acid dominated the initial reaction pathway before the carboxylic acids proceeded into deoxygenation via decarbonylation to form hydrocarbon. Reaction without catalyst and using interparticle mesopore ZSM-5_T catalysts produced short-chain carboxylic acids due to the restricted diffusion. The interparticle mesoporosity on Ni/ZSM-5_T is
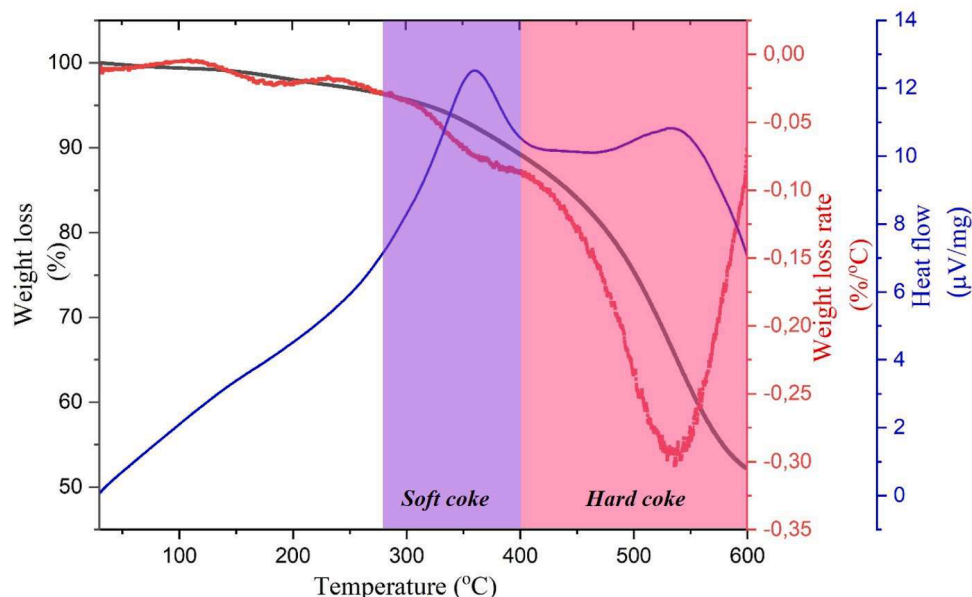

Fig. 12. TGA-DTG-DSC profile of spent catalyst 10%Ni/Al-MCM-41.

suggested to dissipate upon dispersion of catalysts in oil, thus reducing the mesopore effect during the catalytic reaction. The highest yields of organic liquid products (~38 %) and conversion (80 %) were obtained on Ni/Al-MCM-41 at 350 °C for 4 h reaction under solvent and H_2-free deoxygenation. The highly ordered mesopores Al-MCM-41 and well-defined intraparticle mesopore in ZSM-5_S enhanced the mass transfer of oleic acid, consequently preserving the long carbon chain during the reaction. The resulting carboxylic acid subsequently underwent decarbonylation to generate green diesel hydrocarbon of 88.57 % with a ratio of alkane/alkene of 2.5. ZSM-5 and Al-MCM-41 support in this study results in better C_8–C_{17} (88.57 %) selectivity as compared to γ-Al2O3, β-zeolite, and SBA-15 from previous study. The choice of catalyst support is critical in green diesel production as it affects the feasibility of the process. Future green diesel production should consider catalysts with high mesoporosity and acidity.

CRediT authorship contribution statement

Reva Edra Nugraha: Writing – original draft, Validation, Methodology, Investigation, Conceptualization, Funding acquisition. **Hari Purnomo:** Writing – original draft, Validation, Methodology, Investigation. **Abdul Aziz:** Writing – original draft, Validation, Investigation, Data curation. **Holilah Holilah:** Writing – review & editing, Validation, Investigation, Formal analysis. **Hasliza Bahruji:** Writing – review & editing, Validation, Supervision. **Nurul Asikin-Mijan:** Writing – review & editing, Validation, Investigation. **Suprapto Suprapto:** Writing – review & editing, Validation, Supervision, Funding acquisition. **Yun Hin Taufiq-Yap:** Supervision, Resources. **Aishah Abdul Jalil:** Validation, Resources, Conceptualization. **Hartati Hartati:** Validation, Resources, Conceptualization. **Didik Prasetyoko:** Writing – review & editing, Validation, Supervision, Conceptualization.

Declaration of competing interest

The authors declare that they have no known competing financial interests or personal relationships that could have appeared to influence the work reported in this paper.

Acknowledgements

Supplementary materials

Supplementary material associated with this article can be found, in the online version, at https://doi.org/10.1016/j.sajce.2024.04.009.

References

Abdulkareem-Alsultan, G., Asikin-Mijan, N., Mustafa-Alsultan, G., Lee, H.V., Wilson, K., Taufiq-Yap, Y.H., 2020. Efficient deoxygenation of waste cooking oil over Co3O4-La2O3-doped activated carbon for the production of diesel-like fuel. RSC Adv. 10, 4996–5009. https://doi.org/10.1039/c9ra09516k.

Abidin, S.N.Z., Lee, H.V., Juan, J.C., Rahman, N.A., Taufiq-Yap, Y.H., 2019. Production of green biofuel by using a goat manure supported Ni-Al hydrotalcite catalysed deoxygenation process. RSC Adv. 9, 1642–1652. https://doi.org/10.1039/C8RA07818A.

Abozenadah, H., Bishop, A., Bittner, S., Lopez, O., Wiley, C., Flatt, P.M., 2017. Chapter 7: alkanes and halogenated hydrocarbons. Consumer Chemistry: How Organic Chemistry Impacts Our Lives.

Aghamohammadi, S., Haghighi, M., Ebrahimi, A., 2019. Fabrication of attrition-resistant nanostructured catalyst by spray dryer for methanol to light olefins reaction in a fluid bed reactor and coke formation. Microporous Mesoporous Mater. 279, 371–386. https://doi.org/10.1016/j.micromeso.2019.01.017.

Ainembabazi, D., Reid, C., Chen, A., An, N., Kostal, J., Voutchkova-Kostal, A., 2020. Decarbonylative olefination of aldehydes to alkenes. J. Am. Chem. Soc. 142, 696–699. https://doi.org/10.1021/jacs.9b12354.

Al Muttaqii, M., Marlinda, L., Roesyadi, A., Hari Prajitno, D., 2017. Co-Ni/HZSM-5 catalyst for hydrocracking of sunan candlenut oil (Reutealis trisperma (Blanco) Airy Shaw) for production of biofuel. J. Pure Appl. Chem. Res. 6, 84–92. https://doi.org/10.21776/ub.jpacr.2017.006.02.257.

Alaba, P.A., Sani, Y.M., Mohammed, I.Y., Wan Daud, W.M.A., 2016. Insight into catalyst deactivation mechanism and suppression techniques in thermocatalytic deoxygenation of bio-oil over zeolites. Rev. Chem. Eng. 32, 71–91. https://doi.org/10.1515/revce-2015-0025.

Ali, A., Zhao, C., 2020. Selective synthesis of α-olefins by dehydration of fatty alcohols over alumina-thoria mixed catalysts. Catal. Sci. Technol. 10, 3701–3708. https://doi.org/10.1039/d0cy00551g.

Angelovič, Michal, Jablonický, J., Tkáč, Z., Angelovič, Marek, 2015. Oxidative stability of fatty acid alkyl esters: a review. Potravinarstvo 9, 417–426. https://doi.org/10.5219/500.

Arumugam, M., Goh, C.K., Zainal, Z., Triwahyono, S., Lee, A.F., Wilson, K., Taufiq-yap, Y.H., 2021. Hierarchical hzsm-5 for catalytic cracking of oleic acid to biofuels. Nanomaterials 11, 1–11. https://doi.org/10.3390/nano11030747.

Asikin-Mijan, N., Ooi, J.M., AbdulKareem-Alsultan, G., Lee, H.V., Mastuli, M.S., Mansir, N., Alharthi, F.A., Alghamdi, A.A., Taufiq-Yap, Y.H., 2020. Free-H2 deoxygenation of Jatropha curcas oil into cleaner diesel-grade biofuel over coconut residue-derived activated carbon catalyst. J. Clean. Prod. 249, 119381 https://doi.org/10.1016/j.jclepro.2019.119381.

Asomaning, J., Mussone, P., Bressler, D.C., 2014. Thermal deoxygenation and pyrolysis of oleic acid. J. Anal. Appl. Pyrolysis 105, 1–7. https://doi.org/10.1016/j.jaap.2013.09.005.

Baharudin, K.B., Abdullah, N., Taufiq-Yap, Y.H., Derawi, D., 2020. Renewable diesel via solventless and hydrogen-free catalytic deoxygenation of palm fatty acid distillate. J. Clean. Prod. 274 https://doi.org/10.1016/j.jclepro.2020.122850.

Baharudin, K.B., Taufiq-Yap, Y.H., Hunns, J., Isaacs, M., Wilson, K., Derawi, D., 2019. Mesoporous NiO/Al-SBA-15 catalysts for solvent-free deoxygenation of palm fatty acid distillate. Microporous Mesoporous Mater 276, 13–22. https://doi.org/10.1016/j.micromeso.2018.09.014.

Cakiryilmaz, N., Arbag, H., Oktar, N., Dogu, G., Dogu, T., 2019. Catalytic performances of Ni and Cu impregnated MCM-41 and Zr-MCM-41 for hydrogen production through steam reforming of acetic acid. Catal. Today 323, 191–199. https://doi.org/10.1016/j.cattod.2018.06.004.

Chen, J., Shi, H., Li, L., Li, K., 2014. Deoxygenation of methyl laurate as a model compound to hydrocarbons on transition metal phosphide catalysts. Appl. Catal. B Environ. 144, 870–884. https://doi.org/10.1016/j.apcatb.2013.08.026.

Chen, L., Zhang, F., Li, G., Li, X., 2017a. Effect of Zn/Al ratio of Ni/ZnO-Al2O3 catalysts on the catalytic deoxygenation of oleic acid into alkane. Appl. Catal. A Gen. 529, 175–184. https://doi.org/10.1016/j.apcata.2016.11.012.

Chen, N., Wang, N., Ren, Y., Tominaga, H., Qian, E.W., 2017b. Effect of surface modification with silica on the structure and activity of Pt/ZSM-22@SiO2 catalysts in hydrodeoxygenation of methyl palmitate. J. Catal. 345, 124–134. https://doi.org/10.1016/j.jcat.2016.09.005.

Corma, A., Orchille, A.V., 2000. Current views on the mechanism of catalytic cracking. Microporous Mesoporous Mater 35–36, 21–30.

Corsetti, S., Rabl, T., McGloin, D., Kiefer, J., 2017. Intermediate phases during solid to liquid transitions in long-chain n-alkanes. Phys. Chem. Chem. Phys. 19, 13941–13950. https://doi.org/10.1039/c7cp01468f.

Crawford, J.M., Smoljan, C.S., Lucero, J., Carreon, M.A., 2019. Deoxygenation of stearic acid over cobalt-based nax zeolite catalysts. Catalysts 9, 1–15. https://doi.org/10.3390/catal9010042.

de Barros Dias Moreira, J., Bastos de Rezende, D., Márcia Duarte Pasa, V., 2020. Deoxygenation of Macauba acid oil over Co-based catalyst supported on activated biochar from Macauba endocarp: a potential and sustainable route for green diesel and biokerosene production. Fuel 269, 117253. https://doi.org/10.1016/j.fuel.2020.117253.

de Oliveira Camargo, Mariana, Castagnari Willimann Pimenta, J.L., de Oliveira Camargo, Marília, Arroyo, P.A., 2020. Green diesel production by solvent-free deoxygenation of oleic acid over nickel phosphide bifunctional catalysts: effect of the support. Fuel 281, 118719. https://doi.org/10.1016/j.fuel.2020.118719.

de Sousa Castro, K., Fernando de Medeiros Costa, L., Fernandes, V.J., de Oliveira Lima, R., Mabel de Morais Araújo, A., Sousa de Sant'Anna, M.C., Albuquerque dos Santos, N., Gondim, A.D., 2020. Catalytic pyrolysis (Ni/Al-MCM-41) of palm (Elaeis guineensis) oil to obtain renewable hydrocarbons. RSC Adv 11, 555–564. https://doi.org/10.1039/d0ra06122k.

Deng, W., Wang, X., Lam, C.H., Xiong, Z., Han, H., Xu, J., Jiang, L., Su, S., Hu, S., Wang, Y., Xiang, J., 2022. Evolution of coke structures during electrochemical upgrading of bio-oil. Fuel Process. Technol. 225, 107036 https://doi.org/10.1016/j.fuproc.2021.107036.

Du, C., Yang, H., 2012. Investigation of the physicochemical aspects from natural kaolin to Al-MCM-41 mesoporous materials. J. Colloid Interface Sci. 369, 216–222. https://doi.org/10.1016/j.jcis.2011.12.041.

Feng, F., Wang, L., Zhang, X., Wang, Q., 2019. Selective Hydroconversion of Oleic Acid into Aviation-Fuel-Range Alkanes over Ultrathin Ni/ZSM-5 Nanosheets. Ind. Eng. Chem. Res. 58, 5432–5444. https://doi.org/10.1021/acs.iecr.9b00103.

Forghani, A.A., Lewis, D.M., 2016. Hydro-conversion of oleic acid in bio-oil to liquid hydrocarbons: an experimental and modeling investigation. J. Chem. Technol. Biotechnol. 91, 655–663. https://doi.org/10.1002/jctb.4618.

Guanhua, N., Qian, S., Meng, X., Hui, W., Yuhang, X., Weimin, C., Gang, W., 2019. Effect of NaCl-SDS compound solution on the wettability and functional groups of coal. Fuel 257, 116077. https://doi.org/10.1016/j.fuel.2019.116077.

Gurdeep Singh, H.K., Yusup, S., Quitain, A.T., Abdullah, B., Ameen, M., Sasaki, M., Kida, T., Cheah, K.W., 2020. Biogasoline production from linoleic acid via catalytic cracking over nickel and copper-doped ZSM-5 catalysts. Environ. Res. 186, 109616 https://doi.org/10.1016/j.envres.2020.109616.

Hakkarainen, H., Järvinen, A., Lepistö, T., Salo, L., Kuittinen, N., Laakkonen, E., Yang, M., Martikainen, M.V., Saarikoski, S., Aurela, M., Barreira, L., Teinilä, K., Ihalainen, M., Aakko-Saksa, P., Timonen, H., Rönkkö, T., Jalava, P., 2023. Toxicity of exhaust emissions from high aromatic and non-aromatic diesel fuels using in vitro ALI exposure system. Sci. Total Environ. 890 https://doi.org/10.1016/j.scitotenv.2023.164215.

He, S., Zuur, K., Santosa, D.S., Heeres, A., Liu, C., Pidko, E., Heeres, H.J., 2021. Catalytic conversion of pure glycerol over an un-modified H-ZSM-5 zeolite to bio-based aromatics. Appl. Catal. B Environ. 281, 119467 https://doi.org/10.1016/j.apcatb.2020.119467.

Hermida, L., Zuhairi, A., Rahman, A., 2015. Deoxygenation of fatty acid to produce diesel-like hydrocarbons : a review of process conditions, reaction kinetics and mechanism. Renew. Sustain. Energy Rev. 42, 1223–1233. https://doi.org/10.1016/j.rser.2014.10.099.

Hongloi, N., Prapainainar, P., Prapainainar, C., 2021. Review of green diesel production from fatty acid deoxygenation over Ni-based catalysts. Mol. Catal. 111696 https://doi.org/10.1016/j.mcat.2021.111696.

Hossain, M.Z., Chowdhury, M.B.I., Jhawar, A.K., Xu, W.Z., Charpentier, P.A., 2018. Continuous low pressure decarboxylation of fatty acids to fuel-range hydrocarbons with in situ hydrogen production. Fuel 212, 470–478. https://doi.org/10.1016/j.fuel.2017.09.092.

Huo, X., Huq, N.A., Stunkel, J., Cleveland, N.S., Starace, A.K., Settle, A.E., York, A.M., Nelson, R.S., Brandner, D.G., Fouts, L., St. John, P.C., Christensen, E.D., Luecke, J., Mack, J.H., McEnally, C.S., Cherry, P.A., Pfefferle, L.D., Strathmann, T.J., Salvachúa, D., Kim, S., McCormick, R.L., Beckham, G.T., Vardon, D.R., 2019. Tailoring diesel bioblendstock from integrated catalytic upgrading of carboxylic acids: a "fuel property first" approach. Green Chem. 21, 5813–5827. https://doi.org/10.1039/c9gc01820d.

Jafarzadeh, A., Sohrabnezhad, S., Zanjanchi, M.A., Arvand, M., 2016. Fabrication of MCM-41 fibers with well-ordered hexagonal mesostructure controlled in acidic and alkaline media. J. Solid State Chem. 242, 236–242. https://doi.org/10.1016/j.jssc.2016.07.030.

Jakeria, M.R., Fazal, M.A., Haseeb, A.S.M.A., 2014. Influence of different factors on the stability of biodiesel: a review. Renew. Sustain. Energy Rev. 30, 154–163. https://doi.org/10.1016/j.rser.2013.09.024.

Janampelli, S., Darbha, S., 2021. Selective deoxygenation of fatty acids to fuel-range hydrocarbons over Pt-MOx/ZrO2 (M = Mo and W) catalysts. Catal. Today 375, 174–180. https://doi.org/10.1016/j.cattod.2020.04.020.

Jeon, K.W., Na, H.S., Lee, Y.L., Ahn, S.Y., Kim, K.J., Shim, J.O., Jang, W.J., Jeong, D.W., Nah, I.W., Roh, H.S., 2019. Catalytic deoxygenation of oleic acid over a Ni-CeZrO2 catalyst. Fuel 258, 116179. https://doi.org/10.1016/j.fuel.2019.116179.

John, A., Miranda, M.O., Ding, K., Dereli, B., Ortuno, M.A., Lapointe, A.M., Coates, G.W., Cramer, C.J., Tolman, W.B., 2016. Nickel catalysts for the dehydrative decarbonylation of carboxylic acids to alkenes. Organometallics 35, 2391–2400. https://doi.org/10.1021/acs.organomet.6b00415.

Kochaputi, N., Kongmark, C., Khemthong, P., Butburee, T., Kuboon, S., Worayingyong, A., Faungnawakij, K., 2019. Catalytic behaviors of supported cu, ni, and co phosphide catalysts for deoxygenation of oleic acid. Catalysts 9, 1–12. https://doi.org/10.3390/catal9090715.

Krobkrong, N., Itthibenchapong, V., Khongpracha, P., Faungnawakij, K., 2018. Deoxygenation of oleic acid under an inert atmosphere using molybdenum oxide-based catalysts. Energy Convers. Manag. 167, 1–8. https://doi.org/10.1016/j.enconman.2018.04.079.

Kumar, N., 2017. Oxidative stability of biodiesel: causes, effects and prevention. Fuel 190, 328–350. https://doi.org/10.1016/j.fuel.2016.11.001.

Li, D., Min, H., Jiang, X., Ran, X., Zou, L., Fan, J., 2013. One-pot synthesis of Aluminum-containing ordered mesoporous silica MCM-41 using coal fly ash for phosphate adsorption. J. Colloid Interface Sci. 404, 42–48. https://doi.org/10.1016/j.jcis.2013.04.018.

Li, G., Zhang, F., Chen, L., Zhang, C., Huang, H., Li, X., 2015a. Highly selective hydrodecarbonylation of oleic acid into n-heptadecane on a supported nickel/zinc oxide-alumina catalyst. ChemCatChem 7, 2646–2653. https://doi.org/10.1002/cctc.201500418.

Li, H., Wang, Y., Meng, F., Chen, H., Sun, C., Wang, S., 2016. Direct synthesis of high-silica nano ZSM-5 aggregates with controllable mesoporosity and enhanced catalytic properties. RSC Adv 6, 99129–99138. https://doi.org/10.1039/c6ra21080e.

Li, M., Xing, S., Yang, L., Fu, J., Lv, P., Wang, Z., Yuan, Z., 2019. Nickel-loaded ZSM-5 catalysed hydrogenation of oleic acid: the game between acid sites and metal centres. Appl. Catal. A Gen. 587, 117112 https://doi.org/10.1016/j.apcata.2019.117112.

Li, Y., Zhang, C., Liu, Y., Hou, X., Zhang, R., Tang, X., 2015b. Coke deposition on Ni/HZSM-5 in bio-oil hydrodeoxygenation processing. Energy Fuels 29, 1722–1728. https://doi.org/10.1021/ef5024669.

Luo, W., Cao, W., Bruijnincx, P.C.A., Lin, L., Wang, A., Zhang, T., 2019. Zeolite-supported metal catalysts for selective hydrodeoxygenation of biomass-derived platform molecules. Green Chem 21, 3744–3768. https://doi.org/10.1039/c9gc01216h.

Ma, T., Yun, Z., Xu, W., Chen, L., Li, L., Ding, J., Shao, R., 2016. Pd-H3PW12O40/Zr-MCM-41: an efficient catalyst for the sustainable dehydration of glycerol to acrolein. Chem. Eng. J. 294, 343–352. https://doi.org/10.1016/j.cej.2016.02.091.

Maher, K.D., Bressler, D.C., 2007. Pyrolysis of triglyceride materials for the production of renewable fuels and chemicals. Bioresour. Technol. 98, 2351–2368. https://doi.org/10.1016/j.biortech.2006.10.025.

Monirul, I.M., Masjuki, H.H., Kalam, M.A., Zulkifli, N.W.M., Rashedul, H.K., Rashed, M.M., Imdadul, H.K., Mosarof, M.H., 2015. A comprehensive review on biodiesel cold flow properties and oxidation stability along with their improvement processes. RSC Adv. 5, 86631–86655. https://doi.org/10.1039/c5ra09555g.

Moussa, S., Concepción, P., Arribas, M.A., Martínez, A., 2020. The nature of active Ni sites and the role of Al species in the oligomerization of ethylene on mesoporous Ni-Al-MCM-41 catalysts. Appl. Catal. A Gen. 608, 117831 https://doi.org/10.1016/j.apcata.2020.117831.

Neill, W.S., Chippior, W.L., Gülder, Ö.L., Cooley, J., Richardson, E.K., Mitchell, K., Fairbridge, C., 2000. Influence of fuel aromatics type on the particulate matter and NO x emissions of a heavy-duty diesel engine. SAE Tech. Pap. https://doi.org/10.4271/2000-01-1856.

Niu, S., Zhou, Y., Yu, H., Lu, C., Han, K., 2017. Investigation on thermal degradation properties of oleic acid and its methyl and ethyl esters through TG-FTIR. Energy Convers. Manag. 149, 495–504. https://doi.org/10.1016/j.enconman.2017.07.053.

Nugraha, R.E., Prasetyoko, D., Asikin-Mijan, N., Bahruji, H., Suprapto, S., Taufiq-Yap, Y. H., Jalil, A.A., 2021a. The effect of structure directing agents on micro/mesopore structures of aluminosilicates from Indonesian kaolin as deoxygenation catalysts. Microporous Mesoporous Mater 315, 110917. https://doi.org/10.1016/j.micromeso.2021.110917.

Nugraha, R.E., Prasetyoko, D., Bahruji, H., Suprapto, S., Asikin-Mijan, N., Oetami, T.P., Jalil, A.A., Vo, D.-V.N., Yun Hin, T.-Y., 2021b. Lewis acid Ni/Al-MCM-41 catalysts for H2-free deoxygenation of Reutealis trisperma oil to biofuels. RSC Adv 11, 21885–21896. https://doi.org/10.1039/d1ra03145g.

Oliveira, M.R., Cecilia, J.A., De Conto, J.F., Egues, S.M., Rodríguez-Castellón, E., 2023. Rapid synthesis of MCM-41 and SBA-15 by microwave irradiation: promising adsorbents for CO2 adsorption. J. Sol-Gel Sci. Technol. 105, 370–387. https://doi.org/10.1007/s10971-022-06016-3.

Ooi, X.Y., Oi, L.E., Choo, M.Y., Ong, H.C., Lee, H.V., Show, P.L., Lin, Y.C., Juan, J.C., 2019. Efficient deoxygenation of triglycerides to hydrocarbon-biofuel over mesoporous Al2O3-TiO2 catalyst. Fuel Process. Technol. 194, 106120 https://doi.org/10.1016/j.fuproc.2019.106120.

Palizdar, A., Sadrameli, S.M., 2020. Catalytic upgrading of biomass pyrolysis oil over tailored hierarchical MFI zeolite: effect of porosity enhancement and porosity-acidity interaction on deoxygenation reactions. Renew. Energy 148, 674–688. https://doi.org/10.1016/j.renene.2019.10.155.

Premaratne, W.A.P.J., Priyadarshana, W.M.G.I., Gunawardena, S.H.P., De Alwis, A.A.P., 2014. Synthesis of Nanosilica from Paddy Husk Ash and Their Surface Functionalization. J. Sci. Univ. Kelaniya Sri Lanka 8, 33. https://doi.org/10.4038/josuk.v8i0.7238.

Ramos, M., Dias, A.P.S., Puna, J.F., Gomes, J., Bordado, J.C., 2019. Biodiesel production processes and sustainable raw materials. Energies 12. https://doi.org/10.3390/en12234408.

Riyanto, T., Istadi, I., Jongsomjit, B., Anggoro, D.D., Pratama, A.A., Al Faris, M.A., 2021. Improved brønsted to lewis (B/L) ratio of co-and mo-impregnated ZSM-5 catalysts for palm oil conversion to hydrocarbon-rich biofuels. Catalysts 11. https://doi.org/10.3390/catal11111286.

Rodrigues, B., Shende, P., 2020. Monodispersed metal-based dendrimeric nanoclusters for potentiation of anti-tuberculosis action. J. Mol. Liq. 304, 112731 https://doi.org/10.1016/j.molliq.2020.112731.

Roh, H.S., Eum, I.H., Jeong, D.W., Yi, B.E., Na, J.G., Ko, C.H., 2011. The effect of calcination temperature on the performance of Ni/MgO-Al 2O3 catalysts for decarboxylation of oleic acid. Catal. Today 164, 457–460. https://doi.org/10.1016/j.cattod.2010.10.048.

Santos, M.R., Arias, S., Padilha, J.F., Carneiro, M.C.N., Sales, E.A., Pacheco, J.G.A., Fréty, R., 2020. Catalytic cracking of palmitic and oleic acids pre-adsorbed on γ-alumina. Catal. Today 344, 234–239. https://doi.org/10.1016/j.cattod.2019.04.005.

Shim, J.O., Jeon, K.W., Jang, W.J., Na, H.S., Cho, J.W., Kim, H.M., Lee, Y.L., Jeong, D.W., Roh, H.S., Ko, C.H., 2018. Facile production of biofuel via solvent-free deoxygenation of oleic acid using a CoMo catalyst. Appl. Catal. B Environ. 239, 644–653. https://doi.org/10.1016/j.apcatb.2018.08.057.

Silva, F.C.M., Lima, M.S., Neto, C.O.C., Sá, J.L.S., Souza, L.D., 2018. Catalytic deoxygenation of C18 fatty acids over HAlMCM-41 molecular sieve. Biomass Convers. Biorefinery 8, 159–167. https://doi.org/10.1007/s13399-017-0263-9.

Silva, J.B., Almeida, J.S., Barbosa, R.V., Fernandes, G.J.T., Coriolano, A.C.F., Fernandes, V.J., Araujo, A.S., 2021. Pressurized differential scanning calorimetry and its calculated cetane index. Processes 9, 1–11.

Singh, D., Sharma, D., Soni, S.L., Sharma, S., Kumar Sharma, P., Jhalani, A., 2020. A review on feedstocks, production processes, and yield for different generations of biodiesel. Fuel 262, 116553. https://doi.org/10.1016/j.fuel.2019.116553.

Smoljan, C.S., Crawford, J.M., Carreon, M.A., 2020. Mesoporous microspherical NiO catalysts for the deoxygenation of oleic acid. Catal. Commun. 143, 106046 https://doi.org/10.1016/j.catcom.2020.106046.

Snåre, M., Kubičková, I., Mäki-Arvela, P., Eränen, K., Murzin, D.Y., 2006. Heterogeneous catalytic deoxygenation of stearic acid for production of biodiesel. Ind. Eng. Chem. Res. 45, 5708–5715. https://doi.org/10.1021/ie060334i.

Srifa, A., Faungnawakij, K., Itthibenchapong, V., Viriya-empikul, N., Charinpanitkul, T., Assabumrungrat, S., 2014. Production of bio-hydrogenated diesel by catalytic hydrotreating of palm oil over NiMoS2/γ-Al2O3 catalyst. Bioresour. Technol. 158, 81–90. https://doi.org/10.1016/j.biortech.2014.01.100.

Tan, Y.L., Abdullah, A.Z., Hameed, B.H., 2019. Product distribution of the thermal and catalytic fast pyrolysis of karanja (Pongamia pinnata) fruit hulls over a reusable

silica-alumina catalyst. Fuel 245, 89–95. https://doi.org/10.1016/j.fuel.2019.02.028.

Techopittayakul, T., Echaroj, S., Santikunaporn, M., Asavatesanupap, C., Chen, Y.H., Yuan, M.H., 2019. Kinetic modeling of 1-decene oligomerization to synthetic fuels and base oil over tungstated-zirconia catalyst. React. Kinet. Mech. Catal. 126, 529–546. https://doi.org/10.1007/s11144-018-1485-y.

Thommes, M., Kaneko, K., Neimark, A.V., Olivier, J.P., Rodriguez-Reinoso, F., Rouquerol, J., Sing, K.S.W., 2015. Physisorption of gases, with special reference to the evaluation of surface area and pore size distribution (IUPAC Technical Report). Pure Appl. Chem. 87, 1051–1069. https://doi.org/10.1515/pac-2014-1117.

Tran, N.T.T., Uemura, Y., Chowdhury, S., Ramli, A., 2016. Vapor-phase hydrodeoxygenation of guaiacol on Al-MCM-41 supported Ni and Co catalysts. Appl. Catal. A Gen. 512, 93–100. https://doi.org/10.1016/j.apcata.2015.12.021.

Unlu, D., Boz, N., Ilgen, O., Hilmioglu, N., 2018. Improvement of fuel properties of biodiesel with what is so different about Was ist so anders am Neuroenhancement ? Open Chem 1, 1–6.

Wang, B., Han, C., Zhang, Q., Li, C., Yang, C., Shan, H., 2015. Studies on the preliminary cracking of heavy oils: the effect of matrix acidity and a proposal of a new reaction route. Energy Fuels 29, 5701–5713. https://doi.org/10.1021/acs.energyfuels.5b01280.

Wang, F., Zhang, W., Jiang, J., Xu, J., Zhai, Q., Wei, L., Long, F., Liu, C., Liu, P., Tan, W., He, D., 2020. Nitrogen-rich carbon-supported ultrafine MoC nanoparticles for the hydrotreatment of oleic acid into diesel-like hydrocarbons. Chem. Eng. J. 382, 122464 https://doi.org/10.1016/j.cej.2019.122464.

Xing, S., Lv, P., Zhao, C., Li, M., Yang, L., Wang, Z., Chen, Y., Liu, S., 2018. Solvent-free catalytic deoxygenation of oleic acid via nano-Ni/HZSM-5: effect of reaction medium and coke characterization. Fuel Process. Technol. 179, 324–333. https://doi.org/10.1016/j.fuproc.2018.07.024.

Yıldız, A., Goldfarb, J.L., Ceylan, S., 2020. Sustainable hydrocarbon fuels via "one-pot" catalytic deoxygenation of waste cooking oil using inexpensive, unsupported metal oxide catalysts. Fuel 263, 116750. https://doi.org/10.1016/j.fuel.2019.116750.

Yoosuk, B., Sanggam, P., Wiengket, S., Prasassarakich, P., 2019. Hydrodeoxygenation of oleic acid and palmitic acid to hydrocarbon-like biofuel over unsupported Ni-Mo and Co-Mo sulfide catalysts. Renew. Energy 139, 1391–1399. https://doi.org/10.1016/j.renene.2019.03.030.

Yulia, D., Zulys, A., 2020. Hydroprocessing of kemiri sunan oil (reutealis trisperma (blanco) airy shaw) over NiMoCe/γ-Al2O3 catalyst to produce green diesel. IOP Conf. Ser. Mater. Sci. Eng. 763 https://doi.org/10.1088/1757-899X/763/1/012038.

Zhang, H., Shao, S., Xiao, R., Shen, D., Zeng, J., 2014. Characterization of coke deposition in the catalytic fast pyrolysis of biomass derivates. Energy Fuels 28, 52–57. https://doi.org/10.1021/ef401458y.